Theor Chem Acc (2010) 127:95–108
DOI 10.1007/s00214-009-0708-8

REGULAR ARTICLE

Heterogeneous reaction mechanisms of the reduction of nitric oxide on carbon surfaces: a theoretical analysis

Ana Arenillas · Borja Arias · Fernando Rubiera · José J. Pis · Ramón López · Pablo Campomanes · Covadonga Pevida · M. Isabel Menéndez

Received: 9 July 2009 / Accepted: 23 November 2009 / Published online: 11 December 2009

Abstract The mechanism of reaction between NO and two models of carbonaceous materials with active sites was investigated at the UB3LYP/6-31 + G(d) and UM06-2X theory levels. The small model is the anthracene radical and the large one is also a monoradical built with ten benzene rings. The mechanistic routes found with both models lead to a satisfactory justification of the experimental data and showed the important role of the temperature and the oxygen and nitrogen surface complexes, generated in the carbonaceous material at intermediate steps of the mechanism, in the global process. The computational results presented in this work revealed that, at low temperatures, the high Gibbs energy barrier that appears after N_2 release from the $(NO)_2$ dimer, initially chemisorbed on the char surface, prevents the subsequent evolution of the system with the result that CO_2 emission does not take place. On the other hand, at high temperatures, the mean energy available to the reactants may be sufficient to overcome this energy barrier giving rise to the formation of N_2 and CO_2 as reduction products. The N_2 may come from two sources depending on the approach of the NO molecule at different points of the reaction coordinate. The best description of the carbonaceous surface through a larger model confirms the absence of N_2O release in the reduction of nitric oxide on carbon surfaces.

Keywords NO heterogeneous reduction · Carbonaceous surface · Reaction mechanisms · Density functional calculations

1 Introduction

The reduction of nitrogen oxide (NO) by carbonaceous materials has been widely investigated by many researchers in relation to the NOx and/or N_2O emissions during coal combustion [1–5]. The global NO heterogeneous reduction can be schematized as follows:

$$C_{ac} + xNO \rightarrow (x/2)\ N_2 + CO_x \quad (1)$$

or

$$C_{ac} + xNO \rightarrow (x/2)\ N_2O + (1/2)\ CO_x \quad (2)$$

where C_{ac} represents an active site on the char surface. However, the mechanisms involved in the process are not yet fully understood. Ever since the work of Smith et al. in 1959 [6] to the present day, two generally accepted conclusions about the mechanism of the NO-carbon reaction have been drawn from experimental observations: (1) first step is chemisorption of NO on the carbon surface, and (2) oxygen complexes are important intermediates in the reaction. Published works on this subject agree that reduction goes through two stages: NO adsorption, reversibly

Electronic supplementary material The online version of this article (doi:10.1007/s00214-009-0708-8) contains supplementary material, which is available to authorized users.

A. Arenillas · B. Arias · F. Rubiera · J. J. Pis · C. Pevida (✉)
Instituto Nacional del Carbón, CSIC,
Apartado 73, 33080 Oviedo, Spain
e-mail: cpevida@incar.cisc.es

R. López · M. I. Menéndez (✉)
Departmento de Química Física y Analítica,
Universidad de Oviedo, C/Julián Clavería 8,
33006 Oviedo, Spain
e-mail: Isabel@uniovi.es

P. Campomanes
Laboratory of Computational Chemistry and Biochemistry,
École Polytechnique Fédérale de Lausanne (EPFL),
1015 Lausanne, Switzerland

and/or irreversibly, at low temperatures (i.e. <523.15 K), and NO-char reaction at higher temperatures. However, it should be borne in mind that no stage is independent, as NO adsorption influences the NO-char gasification process.

It is clear that in spite of the experimental [1–5, 7–12] and theoretical [13–18] works already published, further research is required in order to clarify certain important matters, namely, the features of NO adsorption on the carbon surface, and the routes for N_2, N_2O, CO, and CO_2 formation during the NO heterogeneous reduction on carbon surfaces.

Previous works on this subject have been carried out using a *synthetic coal char* [7–11]. Coal has a very complex and heterogeneous structure, which makes it difficult to isolate the factors influencing the release of NO_X during coal combustion. Attempts have been made to clarify the reaction mechanism using several experimental techniques such as temperature-programmed reduction (TPR) tests and step response experiments with isotopically labeled ^{15}NO [5, 7, 8]. The results obtained have shown that the global reaction is complex and that temperature plays a determining role in the reaction mechanism. N_2 and CO_2 have been revealed as the main reduction products, being possible to schematize the global NO–C reactions as follows:

$$C_{ac} + 2NO \rightarrow CO_2 + N_2 \quad (3)$$

where C_{ac} represents the active centers on the char surface.

It has also been found that low temperature (<523.15 K) NO–C reactions are governed by NO chemisorption on the carbon surface with the formation of oxygen surface complexes and N_2 release. Thus, with the formation of a dimer [9] the chemisorption step could be schematized by the following sequence of reactions:

$$C_{ac} + (NO)_2 \rightarrow N_2 + C(O_2) \quad (4)$$

$$C_{ac} + (NO)_2 \rightarrow 2C(N) + C(O_2). \quad (5)$$

It has also been found that a significant amount of nitrogen is trapped on the carbon during the C-NO reaction. The formation of N_2 from this reaction could be ascribed mainly to the reaction between the surface nitrogen species, C(N), and gaseous NO.

As the temperature increases, the gasification reaction becomes more relevant than the chemisorption of NO on the carbon surface. Oxygen complexes on the char surface desorb as CO_2 creating new sites for reaction with NO. However, the lower the temperature, the lower the extent of desorption of these complexes, as a result of which they may prevent the NO from attacking the char surface. Thus, these reactions depend strongly on the operating temperature, which controls desorption of the oxygen surface complexes:

$$C(O_2) \rightarrow CO_2 + C_{ac}. \quad (6)$$

Nitrogen surface complexes are thermally more stable than oxygen surface complexes and so they can remain on the surface at moderate temperatures. In general, it was found that the higher the temperature, the greater the number of sites susceptible to NO chemisorption and therefore to C(N) formation.

Step response experiments have been performed at high temperatures [5], between 1,023.15 and 1,273.15 K, showing the formation of nitrogen surface complexes, C(N), which could be the real intermediates in the NO–C reaction. Therefore, the formation of N_2 in this temperature range could be explained as follows:

$$C(N) + NO \rightarrow N_2 + C(O). \quad (7)$$

A direct reaction between two C(N) groups to form N_2 is not very probable in the light of our previous experimental results [5].

The global NO heterogeneous reduction mechanism in the high-temperature range (1,023.15–1,273.15 K) has been explained by a combination of two factors. On the one hand, NO attacks the char-forming surface complexes and, on the other, desorption of these complexes, especially those that are oxygenated, resulting in the formation of new sites of reaction. The following sequence of reactions summarizes the process:

$$2C_{ac} + NO \rightarrow C(N) + C(O) \quad (8)$$

$$C(N) + NO \rightarrow N_2 + C(O) \quad (9)$$

$$C_{ac} + C(O) + NO \rightarrow C(O_2) + C(N) \quad (10)$$

$$C(O_2) \rightarrow CO_2 + C_{ac} \quad (11)$$

where the role of nitrogen and oxygen surface complexes as the real reaction intermediates is evident.

Some other authors have detected N_2O as gaseous products from the heterogeneous reduction of NO [1], even where there is no oxygen in the reacting gas. However, under the experimental conditions used in our previous works [5, 8], these gases have not been detected. The reason for this and other matters such the validation of the proposed mechanisms mentioned above, based on experimental data, will be treated in the present work.

The combination of theoretical calculations with the experimental findings may verify the mechanisms involved in the formation of N_2 and CO_2 during the heterogeneous reduction of NO on carbon surfaces, the role of the intermediate surface complexes, and the extensive influence of temperature on the reactions. To this end, in the present work, we undertake a theoretical study of the reaction between NO and two zig-zag models of a carbonaceous material with only one active site, the anthracene radical and a larger monoradical model built with ten benzene rings (see Fig. 1). Among various models of carbonaceous surface, we select the zig-zag type as one of the most invoked in the literature [15–18]. Besides, this mechanistic investigation involves, for the first time, the location of

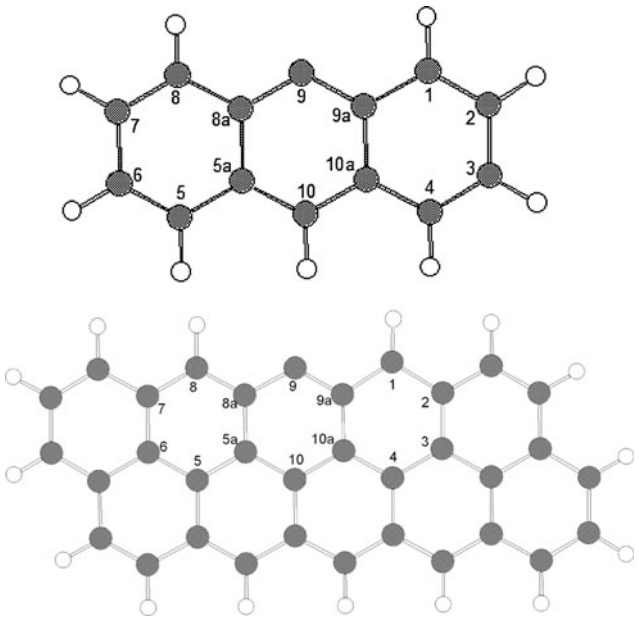

Fig. 1 Molecular numbering of the radicals considered in this work

transition states (TSs), which significantly increases the computational effort, particularly in the most realistic model employed by us, and the quality of kinetic information attainable.

2 Methods

Quantum chemical computations were performed with the Gaussian 03 [19] and Gaussian 09 [20] series of programs. All the critical structures were fully optimized by means of the UB3LYP [21–23] and UM06-2X [24] density functional theory (DFT) methods using the 6-31 + G(d) basis set [25] and Schlegel's algorithm [26]. UB3LYP calculations have been demonstrated to be adequate for the theoretical treatment of this kind of systems [16–18], while M06-2X is a hybrid meta functional recently developed with excellent performance for main group chemistry and for the description of aromatic systems similar to those used in this work [24, 27, 28]. ROMP2-FC/6-31 + G(d)// UB3LYP/6-31 + G(d) single point calculations were also performed for selected structures in order to calibrate DFT results. Analytical computations of harmonic vibrational frequencies at this theory level were carried out in order to characterize the critical points found and to evaluate its zero-point vibrational energy (ZPVE).

Intrinsic reaction coordinate calculations were performed to check the connection between the TSs and the minimum energy structures using the Gonzalez and Schlegel method [29, 30] implemented in Gaussian series.

Basis set superposition error (BSSE) was calculated at UB3LYP/6-31 + G(d) theory level by using the counterpoise correction [31, 32] method with the Gaussian03 program, for the steps in which one molecule is released or adsorbed.

ΔG values were also calculated at several temperatures assuming the ideal gas, rigid rotor, and harmonic oscillator approximations [33]. A pressure of 1 atm and temperatures of 473.15 and 1,073.15 K were assumed in the calculations.

3 Results and discussion

3.1 Reaction mechanisms

Two models of the carbon surface were used in the present work to investigate the heterogeneous reaction mechanisms on the reduction of nitric oxide. The small one was chosen for an initial study as it shows the essential issues we want to model (it has got one active site in a zig-zag surface border) but requires less computational effort. Based on these results, we enlarged the surface model to achieve more realistic conclusions.

3.1.1 Anthracene radical as model of carbonaceous material

The UB3LYP optimized geometries of the critical structures located for the reaction between NO and the anthracene radical are displayed in Figs. 2, 3, 4 and the corresponding energy data are presented in Table 1 and Table 1S in Supporting Information. Unless otherwise stated the UB3LYP/6-31 + G(d) electronic energies will be reported in the text. A prime symbol (′) will be placed immediately after the structure acronyms to denote that the energy contribution of the N_2 and/or CO_2 molecules already released and/or that of the NO molecules, which will be subsequently added, is included (see Table 1).

Experimental evidences show that the initial step of this reaction must be the dimerization of NO on the carbon surface, so the discussion of the results begins with the complex formed between the NO dimer and the anthracene radical, **M1** (see Fig. 2).

From **M1′**, whose spin density is completely delocalized over the carbon surface, the system evolves through the TS **TS1′**, 5.5 kcal mol^{-1} less stable than **M1′**. At **TS1′** both N–O bonds break, resulting in the formation of oxygen complexes on the carbon surface with the simultaneous release of one N_2 molecule to reach the intermediate **M2′**. This intermediate is 83.6 kcal mol^{-1} more stable than **M1′**, and leads to **M3′** (−44.7 kcal mol^{-1}) through a TS, **TS2′**, for the addition of one NO molecule after surmounting an energy barrier of 43.4 kcal mol^{-1}. The NO addition takes

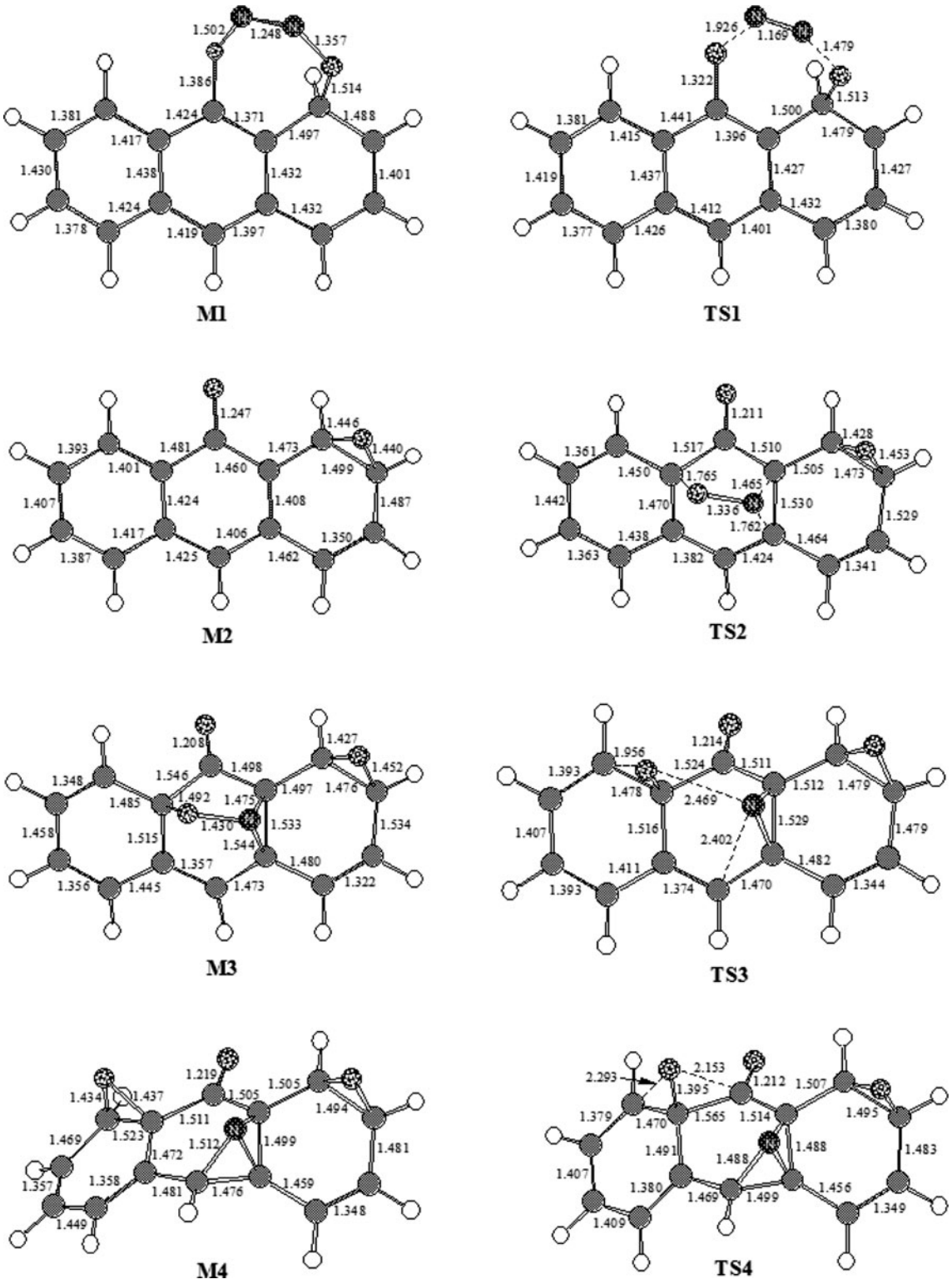

Fig. 2 UB3LYP/6-31 + G(d) optimized geometries corresponding to the first part of the mechanism (from **M1** to **M8**) for the reaction between the anthracene radical **1** and NO. Distances are given in angstroms

place from the top of surface basal plane with the NO bond axis parallel to the surface. This resembles the adsorption direction proposed for the O_2 addition on a single grapheme layer from semiempirical calculations [34]. From **M3′** the breaking of the N–O bond gives rise to the intermediate **M4′** (-40.9 kcal mol^{-1}) through the TS

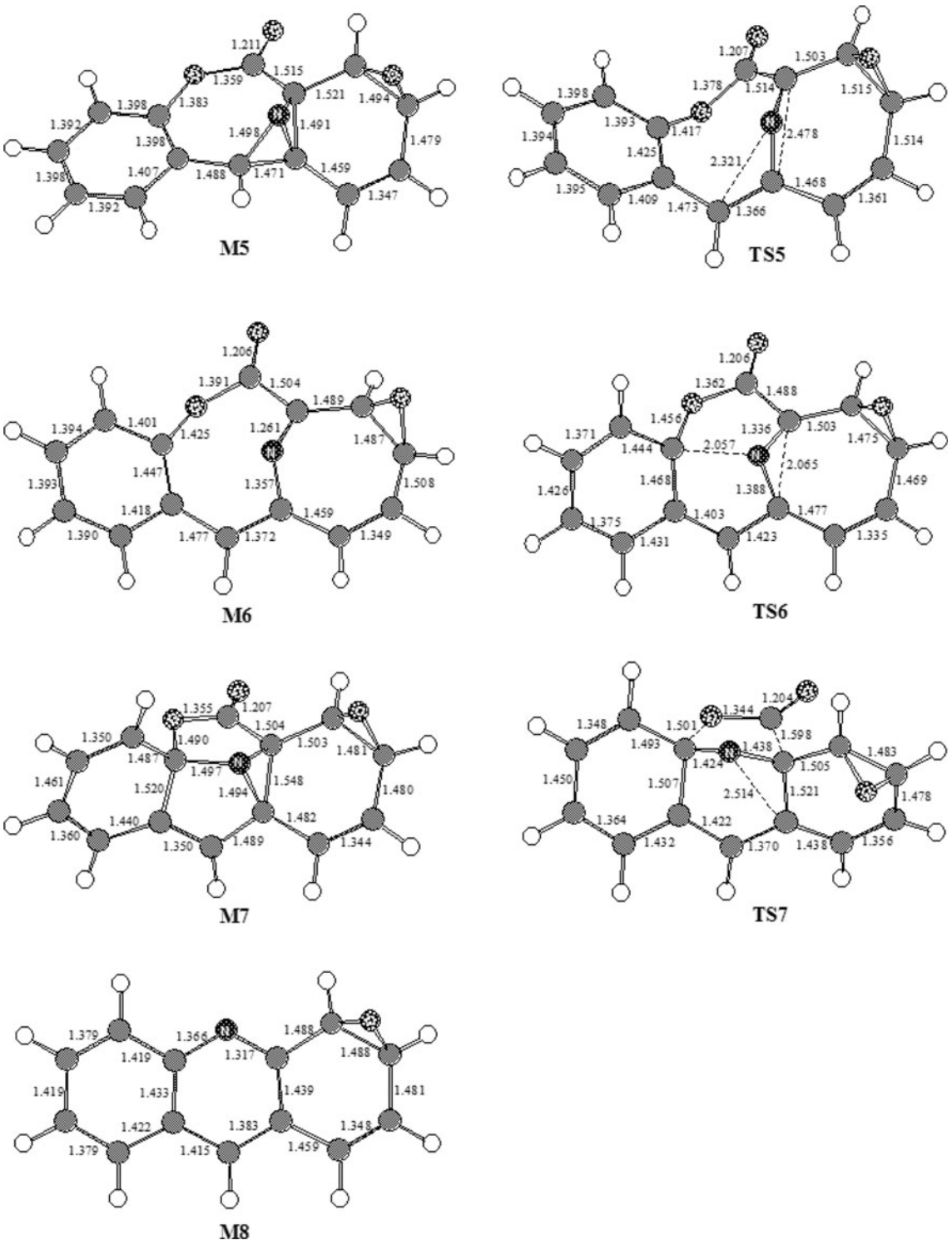

Fig. 2 continued

TS3′. This step also presents a high-energy barrier of 47.9 kcal mol^{-1}.

From **M4′**, the evolution of the system through the TS **TS4′** with an energy barrier of 36.3 kcal mol^{-1} for the insertion of the oxygen atom from the NO moiety into the C_{8a}–C_9 bond (see Fig. 1 for atom numbering) leads to the intermediate **M5′** (−81.5 kcal mol^{-1}). A TS, **TS5′** (−71.1 kcal mol^{-1}), for the insertion of the nitrogen atom into the C_{9a}–C_{10a} bond connects **M5′** with the intermediate **M6′** (−78.4 kcal mol^{-1}). The latter has a flexible eight-

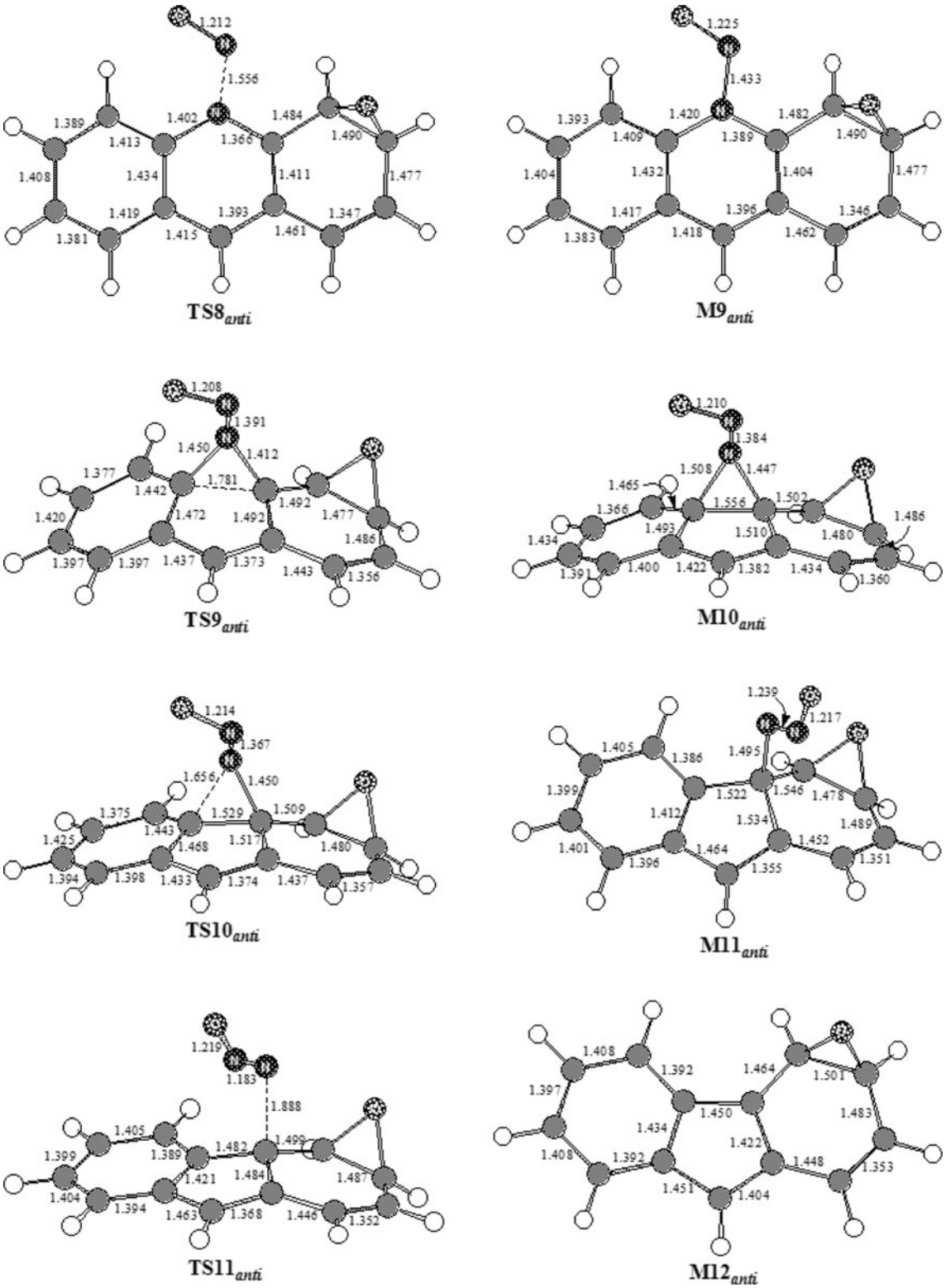

Fig. 3 UB3LYP/6-31 + G(d) optimized geometries corresponding to the *anti* approach between **M8** and NO to give $\mathbf{M12}_{anti}$ + N_2O. Distances are given in angstroms

membered central ring that facilitates the subsequent attack of the N atom on the C_{8a} atom through the TS **TS6′** (−57.6 kcal mol^{-1}) giving rise to the minimum energy structure **M7′** (−83.5 kcal mol^{-1}). **M7′** renders **M8′**, which is 88.6 kcal mol^{-1} below it, through the TS **TS7′** (−71.1 kcal mol^{-1}) releasing one CO_2 molecule and

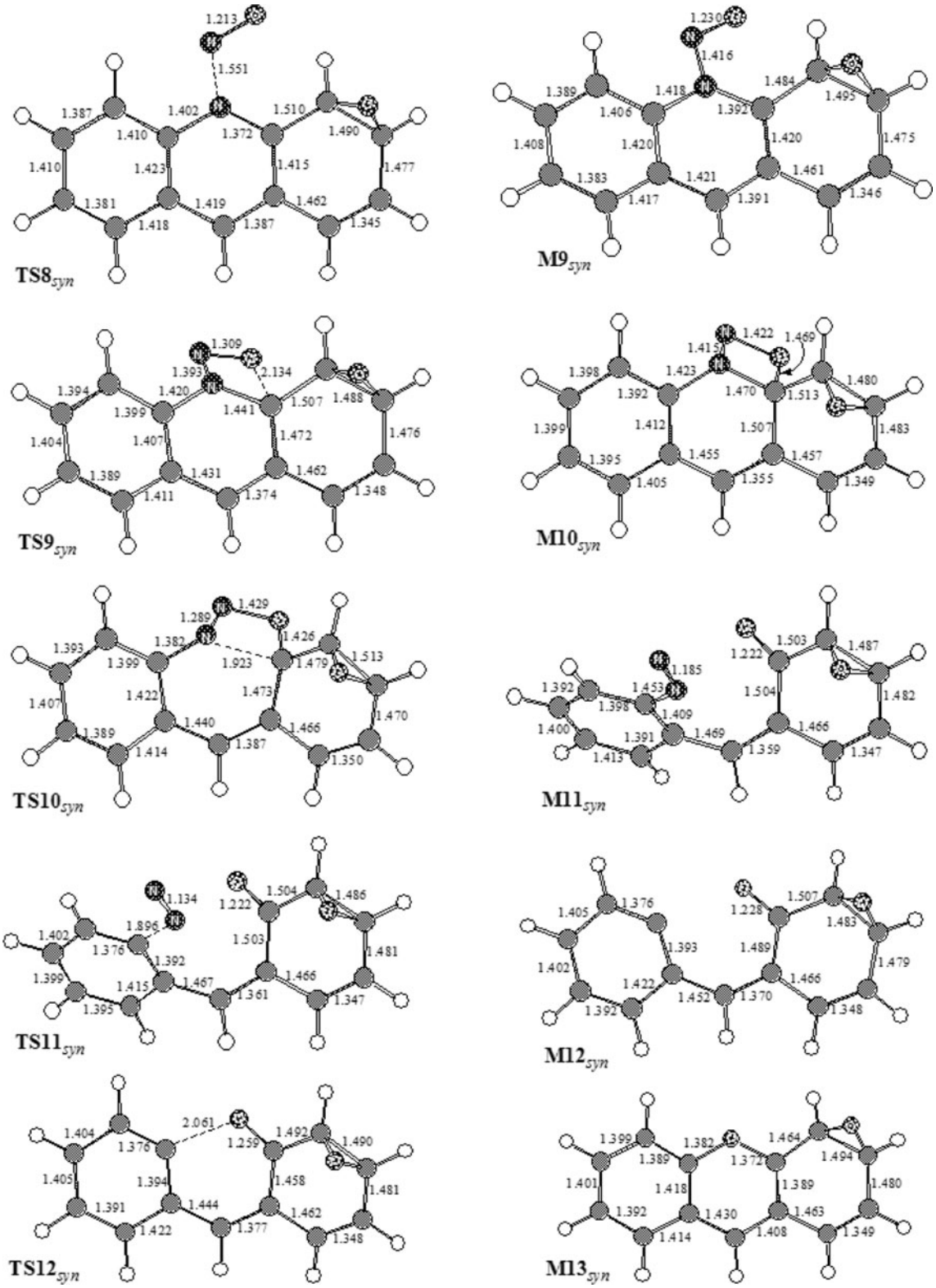

Fig. 4 UB3LYP/6-31 + G(d) optimized geometries corresponding to the *syn* approach between **M8** and NO to give $\mathbf{M13}_{syn}$ + N_2. Distances are given in angstroms

Table 1 UB3LYP/6-31 + G(d)/UM06-2X/6-31 + G(d) relative electronic energies (ΔE_{elec}), and relative Gibbs energies at 473.15 K ($\Delta G_{473.15}$) and 1073.15 K ($\Delta G_{1,073.15}$) for the critical structures located for the reaction between the anthracene radical, 1, and NO

Structures	ΔE_{elec}	$\Delta G_{473.15}$	$\Delta G_{1,073.15}$
M1′ = **M1** + 2NO	0.0/0.0	0.0/0.0	0.0/0.0
TS1′ = **TS1** + 2NO	5.5/15.4	2.8/12.0	1.9/10.8
M2′ = **M2** + 2NO + N_2	−83.6/−87.7	−102.6/−107.4	−125.0/−130.6
TS2′ = **TS2** + NO + N_2	−40.2/−52.9	−37.6/−52.8	−32.9/−49.6
M3′ = **M3** + NO + N_2	−44.7/−65.5	−40.8/−61.4	−36.4/−57.0
TS3′ = **TS3** + NO + N_2	3.2/−16.8	4.4/−16.9	8.0/−14.8
M4′ = **M4** + NO + N_2	−40.9/−68.5	−37.2/−64.7	−33.4/−60.8
TS4′ = **TS4** + NO + N_2	−4.6/−19.0	−3.3/−18.3	0.4/−15.2
M5′ = **M5** + NO + N_2	−81.5/−105.5	−78.0/−102.3	−75.0/−99.8
TS5′ = **TS5** + NO + N_2	−71.1/−85.3	−68.9/−83.7	−65.5/−80.9
M6′ = **M6** + NO + N_2	−78.4/−91.2	−77.1/−90.0	−76.8/−89.8
TS6′ = **TS6** + NO + N_2	−57.6/−68.1	−55.1/−66.1	−50.3/−61.9
M7′ = **M7** + NO + N_2	−83.5/−106.7	−78.8/−102.1	−73.8/−97.5
TS7′ = **TS7** + NO + N_2	−71.1/−85.1	−66.7/−82.0	−60.0/−76.3
M8′ = **M8** + NO + N_2 + CO_2	−172.1/−179.1	−187.7/−194.7	−207.3/−214.2
TS8′$_{anti}$ = **TS8**$_{anti}$ + N_2 + CO_2	−150.5/−154.1	−149.0/−153.3	−147.5/−151.9
M9′$_{anti}$ = **M9**$_{anti}$ + N_2 + CO_2	−150.9/−157.5	−149.1/−155.2	−148.8/−153.9
TS9′$_{anti}$ = **TS9**$_{anti}$ + N_2 + CO_2	−93.3/−103.6	−92.7/−102.7	−90.9/−100.3
M10′$_{anti}$ = **M10**$_{anti}$ + N_2 + CO_2	−96.1/−108.0	−95.7/−107.1	−95.7/−106.4
TS10′$_{anti}$ = **TS10**$_{anti}$ + N_2 + CO_2	−95.2/−104.1	−94.9/−103.5	−93.3/−101.6
M11′$_{anti}$ = **M11**$_{anti}$ + N_2 + CO_2	−130.7/−139.8	−129.6/−138.3	−130.2/−138.5
TS11′$_{anti}$ = **TS11**$_{anti}$ + N_2 + CO_2	−117.8/−123.1	−118.2/−123.1	−118.4/−122.7
M12′$_{anti}$ = **M12**$_{anti}$ + N_2 + CO_2 + N_2O	−153.3/−154.0	−167.9/−168.2	−184.7/−183.8
TS8′$_{syn}$ = **TS8**$_{syn}$ + N_2 + CO_2	−150.0/−154.5	−148.8/−153.4	−147.6/−151.7
M9′$_{syn}$ = **M9**$_{syn}$ + N_2 + CO_2	−151.0/−158.3	−148.9/−155.4	−148.2/−153.6
TS9′$_{syn}$ = **TS9**$_{syn}$ + N_2 + CO_2	−113.7/−120.3	−110.5/−116.9	−106.3/−112.4
M10′$_{syn}$ = **M10**$_{syn}$ + N_2 + CO_2	−122.6/−135.4	−118.6/−131.1	−115.5/−127.6
TS10′$_{syn}$ = **TS10**$_{syn}$ + N_2 + CO_2	−90.0/−95.6	−88.9/−94.0	−86.2/−90.5
M11′$_{syn}$ = **M11**$_{syn}$ + N_2 + CO_2	−158.6/−168.3	−161.1/−170.1	−166.2/−174.2
TS11′$_{syn}$ = **TS11**$_{syn}$ + N_2 + CO_2	−149.0/−158.0	−154.0/−162.0	−159.9/−166.6
M12′$_{syn}$ = **M12**$_{syn}$ + 2N_2 + CO_2	−164.2/−172.0	−185.0/−193.1	−210.6/−218.9
TS12′$_{syn}$ = **TS12**$_{syn}$ + 2N_2 + CO_2	−160.2/−164.4	−179.5/−183.8	−200.8/−204.9
M13′$_{syn}$ = **M13**$_{syn}$ + 2N_2 + CO_2	−207.4/−217.8	−224.0/−234.6	−244.4/−254.8

Energies are given in kcal mol^{-1}

placing the nitrogen atom on the same plane as the rest of the molecular skeleton. **M8′** displays both oxygen and nitrogen complexes on the surface of the carbonaceous material and, therefore, this intermediate can react with another NO molecule via two different routes depending on the way the systems approach each other. In both routes the approach of the NO molecules takes place N-down and on the surface nitrogen atom, in good agreement with previous studies [14, 17, 18].

On the first pathway the approach starts with the O atom of the NO molecule far away from the chemisorbed oxygen atom of **M8** (see Fig. 3), whereas on the second pathway the approach occurs with these two oxygen atoms close together (see Fig. 4). The first route (*anti* approach) proceeds from **M8′** to give rise to the stable species **M9′**$_{anti}$ (−150.9 kcal mol^{-1}) through the TS **TS8′**$_{anti}$ for the formation of a N–N bond with an energy barrier of 21.6 kcal mol^{-1}. **M9′**$_{anti}$ transforms into **M10′**$_{anti}$ (−96.1 kcal mol^{-1}) after surmounting a high-energy barrier of 57.6 kcal mol^{-1} through the TS **TS9′**$_{anti}$. At **M10′**$_{anti}$ the NNO moiety is outside the plane of the rest of the molecule and a new C–C bond between the C_{8a} and C_{9a} carbon atoms is completely formed, giving rise to a highly strained three-member cycle and a five-member one. The release of the strain energy accumulated in this intermediate takes place rapidly through the TS **TS10′**$_{anti}$ for the breaking of one of the C–N bonds with an energy barrier of only 0.9 kcal mol^{-1} yielding the intermediate **M11′**$_{anti}$ (−130.7 kcal mol^{-1}) that in turn evolves through **TS11′**$_{anti}$ (−117.8 kcal mol^{-1}) for the rupture of the remaining C–N bond eliminating a N_2O molecule to give **M12′**$_{anti}$. The second route (*syn* approach) proceeds from **M8′** through

the TS **TS8′$_{syn}$** to render the intermediate **M9′$_{syn}$** (−151.0 kcal mol^{-1}) in which the N–N bond is already formed, the spin-unpaired electron being delocalized between the C atoms on the surface and the oxygen atom of the original NO radical. As expected, both the spin density rearrangement and the energy barrier corresponding to this step (22.1 kcal mol^{-1}) are very similar to those of the **M8′** to **M9′$_{anti}$** transformation. From **M9′$_{syn}$** the system evolves through the TS **TS9′$_{syn}$**, 37.3 kcal mol^{-1} less stable than **M9′$_{syn}$**, to create a C–O bond between the C_{9a} atom and the O atom of the NO moiety to reach the intermediate **M10′$_{syn}$** (−122.6 kcal mol^{-1}) in which a new four-member cycle is created as a result. Interestingly, at this point of the reaction coordinate, the spin density does not extend over the carbonaceous surface, the spin-unpaired electron being highly localized on the N_2O moiety. The concerted and asynchronous breaking of the N–C and N–O bonds leads from **M10′$_{syn}$** to **M11′$_{syn}$** (−158.6 kcal mol^{-1}) through the TS **TS10′$_{syn}$**. At **TS10′$_{syn}$** the N–C bond is clearly elongated (1.923 Å), whereas the distance between N and O is 1.429 Å (see Fig. 4). The formation of the radical species **M11′$_{syn}$**, whose spin density is mainly localized on the N_2 fragment, from **M10′$_{syn}$** presents an energy barrier of 32.6 kcal mol^{-1}. The elimination of the N_2 molecule from **M11′$_{syn}$** takes place through the TS **TS11′$_{syn}$**, 9.6 kcal mol^{-1} above it, yielding an intermediate, **M12′$_{syn}$** (−164.2 kcal mol^{-1}), which rapidly transforms into **M13′$_{syn}$** through the TS **TS12′$_{syn}$** after surmounting an energy barrier of only 4.0 kcal mol^{-1}.

It is remarkable to note that our computations show that a substantial amount of the expected redistribution of the spin density leading to **M12′$_{syn}$** and **M13′$_{syn}$** has already taken place at **TS11′$_{syn}$**, and **TS12′$_{syn}$**, respectively. This early character of both TSs is consistent with the low-energy barriers found for these last two steps of the mechanism.

3.1.2 *Ten condensed benzene rings as a model of the carbonaceous surface*

Figures 1S–4S (in Supporting information) and Fig. 5 collects the UB3LYP/6-31 + G(d) geometries optimized for the large system in which the carbonaceous surface is modeled by a monoradical composed of ten condensed benzene rings, and Table 2 and Table 2S in Supporting information present their corresponding energy data. This large model is more realistic considering both electronic and geometrical aspects as border effects are far away from the active site and fictitious flexibility is absent.

The evolution from **M1′-big** to **M8′-big** (see Figs. 1S and 5) is similar to that from **M1′** to **M8′** in the anthracene radical case except that **M5′-big** undergoes two steps before turning into **M6′-big** (see Fig. 5). In the first of these steps the bond between N and C_{10} is broken through the TS **TS5′-1-big** (4.4 kal mol^{-1} higher in energy than **M5′-big**) to yield **M5′-12-big**. Afterwards, the C_{9a}–C_{10a} bond elongates through **TS5′-2-big** (5.8 kcal mol^{-1} above **M5′-12-big** energy) to get the insertion of N in **M6′-big**.

TS9$_{anti}$ could not be found after an extensive search, so one of the most outstanding effects of the enlargement of the model of the carbonaceous surface is the vanishing of the pathway for the *anti* approach of the NO molecule to **M8′-big** intermediate. The *anti* route found with the small model implies the formation of a five-membered ring with a significant bending of the model, which is not possible in the larger and more realistic model. However, the *syn* approach of the NO molecule is analogous in both models (compare Figs. 4 and 4S).

BSSE has no significant influence on the electronic energy profiles. In effect, the inclusion of this correction increases 1.8 and 2.6 kcal mol^{-1} the electronic energy difference between **TS1′-big** and **M2′-big** (N_2 eliminations) and between **TS7′-big** and **M8′-big** (CO_2 elimination), respectively. Therefore, this implies only small percentages of the relative energies of these intermediates. For the addition of a NO molecule at **M8′-big** this structure becomes 3.1 kcal mol^{-1} more stable when BSSE is included in the calculation.

3.1.3 *Calibration of basis set and density functional*

To check the reliability of the above-mentioned mechanistic predictions on the reduction of NO by carbonaceous surfaces, we also analyzed the effect of a larger basis set (6-311 + G(3df, 2p) and a more elaborated DFT functional (M06-2X).

Concerning the basis set, we focused our attention on the rate-determining step (**M2′** → **TS2′** → **M3′**) of the small system by comparison of UB3LYP/6-31 + G(d) versus UB3LYP/6-311 + G(3df,2p)//UB3LYP/6-31 + G(d) calculations and UM06-2X/6-31 + G(d) versus UM06-2X/6-311 + G(3df,2p)//UM06-2X/6-31 + G(d) ones. For both functionals, in going from 6-31 + G(d) to 6-311 + G(3df,2p) the rate-determining energy barrier slightly increases, 1.7 (UB3LYP) and 0.8 (UM06-2X) kcal mol^{-1}, thus indicating a non-significant effect on the investigated reactive process (see Table 3S in Supporting information).

The effect of replacement of the B3LYP functional by the M06-2X one was analyzed for all the located structures involved in the two selected carbon surface models by performing optimizations and analytical frequency calculations at the UM06-2X/6-31 + G(d) theory level. These optimized geometries are very similar to those found at the UB3LYP/6-31 + G(d) (see Tables 4S and 5S in Supporting information). Tables 1 and 2 and Tables 6S and 7S collect their corresponding relative and absolute electronic energies, respectively. It can be seen that the M06-2X energy

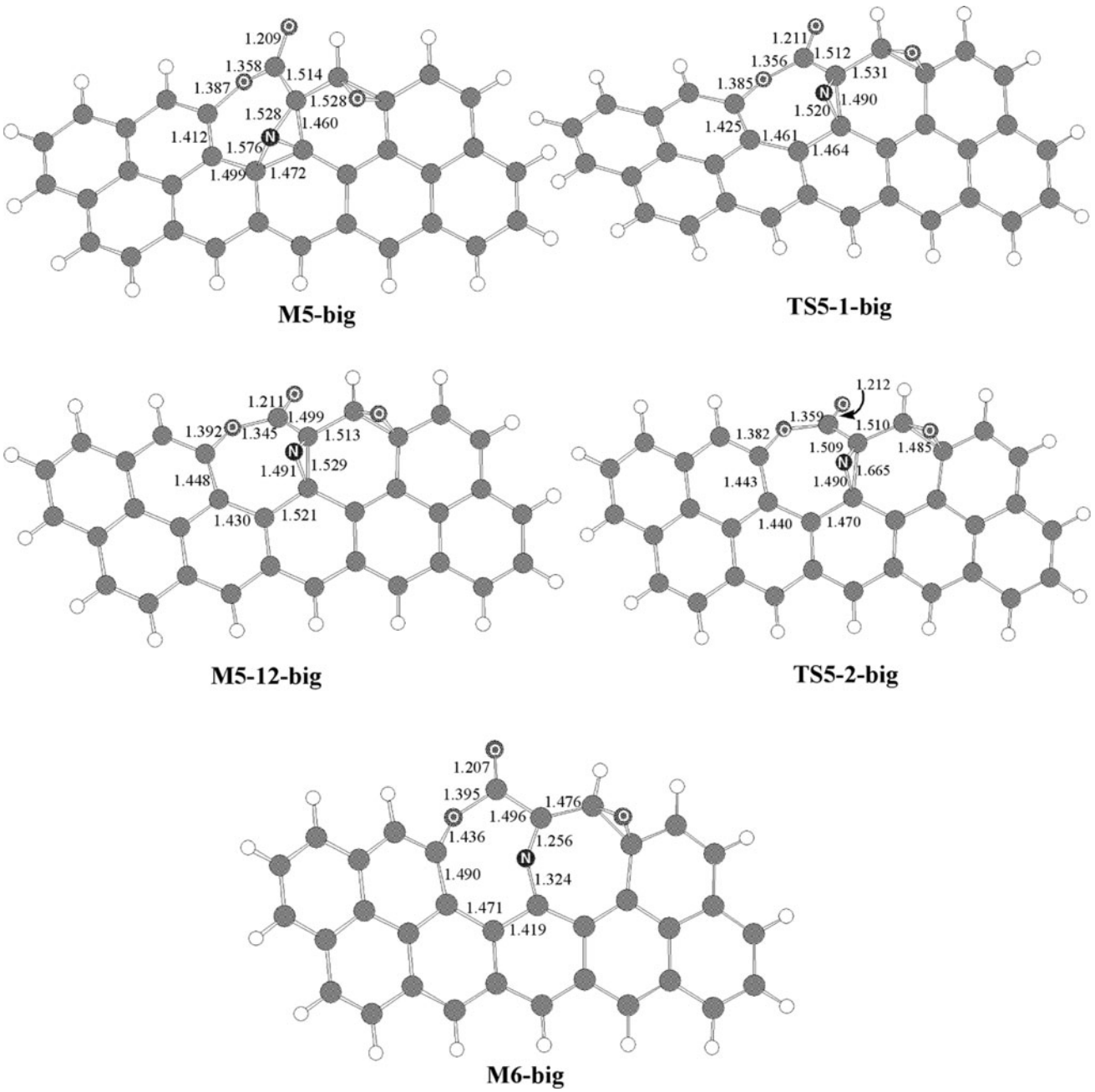

Fig. 5 UB3LYP/6-31 + G(d) optimized geometries corresponding to the new critical structures found for the reaction between the ten benzene radical and NO. Distances are given in Å

profiles for the small and the large systems are displaced to lower values, with the exception of **TS1** and **TS1-big**, for N_2 elimination, which become about 9 kcal mol^{-1} more unstable. Concerning electronic energy barriers, it is interesting to note that most of them rise up when using M06-2X density functional, in a special manner that of **TS4** (increased by 13.2 kcal mol^{-1}), and of **TS4-big** (increased by 20.2 kcal mol^{-1}). Only **TS2** and **TS2-big** show a lowering of 8.6 and 5.6 kcal mol^{-1}, respectively.

Taking into account the energy differences obtained with B3LYP and M06-2X and to go further in the assessment of the accuracy of our DFT results, single point ROMP2-FC/6-31 + G(d)//UB3LYP/6-31 + G(d) calculations were performed for the structures showing more pronounced changes in the small model. Thus, using the MP2 method the energy barrier from **M4** to **TS4** is 46.9 kcal mol^{-1}, and that for **M2** to **TS2** 25.5 kcal mol^{-1}, both closer to M06-2X results than to B3LYP ones. The

Table 2 UB3LYP/6-31 + G(d)/UM06-2X/6-31 + G(d) relative electronic energies (ΔE_{elec}) and relative Gibbs energies at 473.15 ($\Delta G_{473.15}$), and 1,073.15 ($\Delta G_{1,073.15}$) K for the critical structures located for the reaction between the ten benzene rings surface model and NO

Structures	ΔE_{elec}	$\Delta G_{473.15}$	$\Delta G_{1073.15}$
M1′-big = **M1-big** + 2NO	0.0/0.0	0.0/0.0	0.0/0.0
TS1′-big = **TS1-big** + 2NO	5.7/15.1	3.1/11.7	2.6/10.8
M2′-big = **M2-big** + N_2 + 2NO	−73.5/−76.6	−92.6/−96.4	−114.9/−119.3
TS2′-big = **TS2-big** + N_2 + NO	−11.0/−19.7	−10.1/−17.0	−6.5/−12.1
M3′-big = **M3-big** + N_2 +NO	−12.5/−28.2	−9.9/−25.6	−5.9/−21.4
TS3′-big = **TS3-big** + N_2 + NO	14.4/8.9	15.8/9.4	20.2/13.2
M4′-big = **M4-big** + N_2 + NO	−2.2/−28.3	1.0/−24.2	4.5/−20.1
TS4′-big = **TS4-big** + N_2 + NO	27.0/21.1	27.1/21.0	30.4/24.1
M5′-big = **M5-big** + N_2 + NO	−32.6/−55.2	−30.1/−52.3	−27.8/−49.8
TS5′-1-big = **TS5-1-big** + N_2 + NO	−28.2/−41.5	−26.8/−39.2	−23.4/−34.6
M5′-12-big = **M5-12-big** + N_2 +NO	−33.4/−48.7	−32.1/−48.0	−31.4/−46.9
TS5′-2-big = **TS5-2-big** + N_2 +NO	−27.6/−41.5	−26.2/−39.2	−22.6/−34.6
M6′-big = **M6-big** + N_2 + NO	−51.5/−63.0	−50.2/−62.0	−49.5/−61.9
TS6′-big = **TS6-big** + N_2 +NO	−34.1/−45.8	−31.8/−44.9	−26.4/−40.6
M7′-big = **M7-big** + N_2 + NO	−56.3/−68.1	−53.5/−65.1	−49.9/−61.4
TS7′-big = **TS7-big** + N_2 + NO	−55.0/−61.3	−52.6/−59.8	−47.8/−55.8
M8′-big = **M8-big** + N_2 + NO + CO_2	−151.9/−156.9	−167.5/−172.6	−187.0/−191.9
TS8′$_{anti}$-big = **TS8$_{anti}$-big** + N_2 + CO_2	−135.6/−136.3	−134.5/−135.7	−132.6/−134.0
M9′$_{anti}$-big = **M9$_{anti}$-big** + N_2 + CO_2	−138.4/−145.7	−136.1/−142.3	−134.8/−140.0
TS8′$_{syn}$-big = **TS8$_{syn}$-big** + N_2 + CO_2	−134.1/−135.6	−133.3/−134.9	−131.8/−133.0
M9′$_{syn}$-big = **M9$_{syn}$-big** + N_2 + CO_2	−137.8/−145.0	−135.3/−141.9	−133.7/−139.5
TS9′$_{syn}$-big = **TS9$_{syn}$-big** + N_2 + CO_2	−97.8/−102.1	−94.8/−99.0	−90.6/−94.6
M10′$_{syn}$-big = **M10$_{syn}$-big** + N_2 + CO_2	−106.2/−117.7	−102.0/−113.2	−98.4/−109.2
TS10′$_{syn}$-big = **TS10$_{syn}$-big** + N_2 + CO_2	−74.0/−80.8	−72.7/−78.8	−69.4/−74.4
M11′$_{syn}$-big = **M11$_{syn}$-big** + N_2 + CO_2	−137.8/−147.2	−138.8/−148.0	−141.7/−150.3
TS11′$_{syn}$-big = **TS11$_{syn}$-big** + N_2 + O_2	−129.9/−138.7	−133.1/−141.7	−136.5/−144.4
M12′$_{syn}$-big = **M12$_{syn}$-big** + 2N_2 + O_2	−146.5/−154.5	−166.7/−174.1	−191.3/−197.8
TS12′$_{syn}$-big = **TS12$_{syn}$-big** + 2N_2 + O_2	−144.8/−147.8	−164.0/−167.1	−184.9/−187.7
M13′$_{syn}$-big = **M13$_{syn}$-big** + 2N_2 + O_2	−197.5/−207.5	−213.7/−223.8	−233.4/−243.3

Energies are given in kcal mol^{-1}

same trend is observed for all of the remaining structures (see Table 8S in Supporting information).

3.2 Discussion and comparison with the experimental data

In order to compare the theoretical results with the experimental data, the ZPVE, thermal corrections, and entropy determined at two different temperatures (473.15 and 1,073.15 K) were included for both surface models (see Tables 1 and 2, which collect data calculated using B3LYP and M06-2X DFT functionals). For simplicity, only the corresponding Gibbs energy profiles obtained at UM06-2X/6-31 + G(d) are displayed in Figs. 6 and 7. The values of 473.15 and 1,073.15 K were selected as representative examples of the two regimes experimentally studied ($T < 523.15$ K and $T > 1{,}023.15$ K). Unless otherwise indicated, Gibbs energies will be reported in this section.

When including ZPVE, thermal corrections, and entropy in both models (see Tables 1, 2) **M2′**, **M2′-big**, **M12′$_{syn}$** and **M12′$_{syn}$-big** are considerably stabilized mainly due to entropic effects. At these points of the reaction coordinate, N_2 molecules are released from the carbon surface. The same result is obtained at **M8′**, **M8′-big**, due to the extrusion of a CO_2 molecule, and at **M12′$_{anti}$** in the small model.

Concerning relative energies, the large model makes all of the structures more unstable relative to isolated reactants, that is, Gibbs energy profiles at both temperatures are displaced upwards in Fig. 7 with respect to Fig. 6 except for **TS1′** and **TS1′-big**, which remain practically unchanged. But the amount of the displacement is not constant for all the intermediates and TSs. In fact, **TS2′-big**, **M3′-big**, **M4′-big**, **TS4′-big**, **M5′-big**, and the TSs between **M5′-big** and **M6′-big** become destabilized by 30–50 kcal mol^{-1} both at 473.15 and 1,073.15 K, while the remaining structures are destabilized by no more than 20 kcal mol^{-1} at the outside. At **TS2′-big**, **M3′-big** and **M4′-big** important changes in the electronic structure are taking place, as the bonding of a NO molecule through both atoms on the

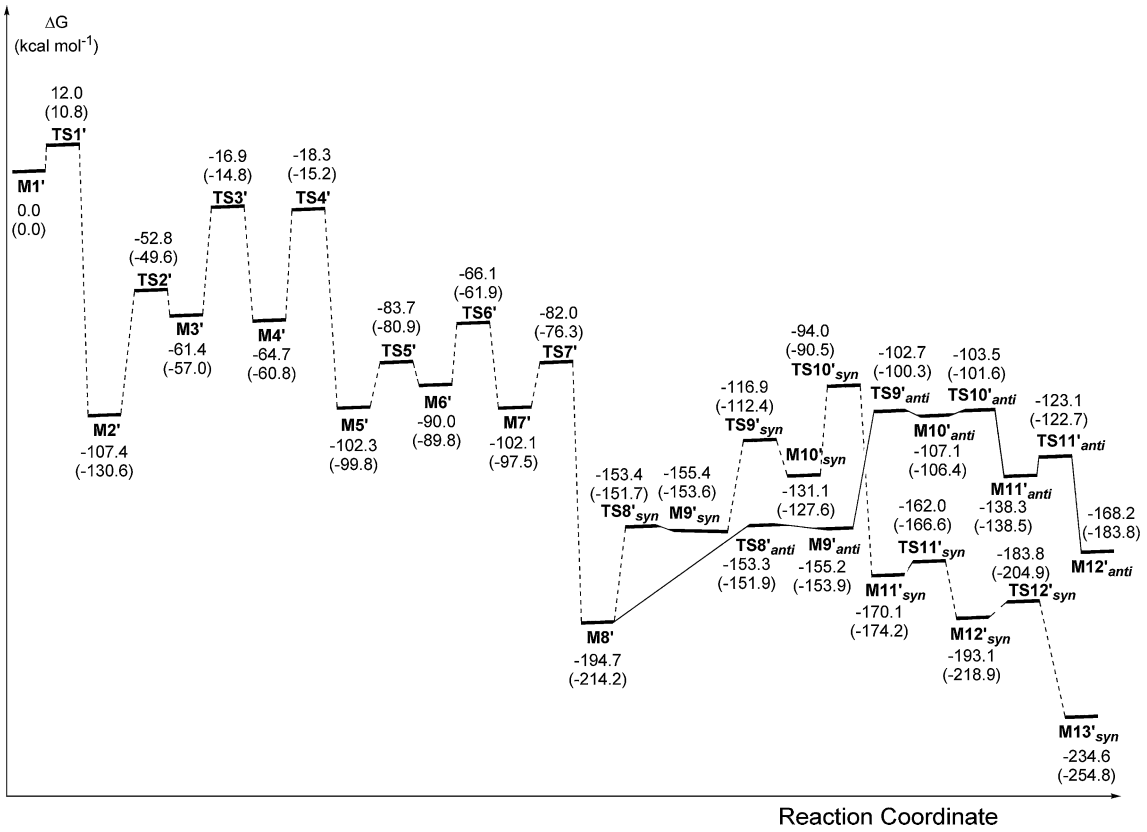

Fig. 6 UM06-2X/6-31 + G(d) Gibbs energy profiles at 473.15 and 1,073.15 K (*in parenthesis*) for the reaction between the anthracene radical **1** and NO

carbonaceous surface disturbs the aromaticity in the O-complex **M2′-big**. On the other hand, the destabilization observed between **TS4′-big** and **M6′-big** can be attributed to the important geometric and electronic changes produced during the insertion of O and N atoms into the carbonaceous material. As main geometric and electronic issues of real carbonaceous surfaces are included in our large model, it could be expected that the data obtained with this model will be close to real ones.

Thus, according to our theoretical calculations, the rate-determining Gibbs energy barrier of the mechanism found at both temperatures (473.15 and 1,073.15 K) corresponds to the evolution of **M2′** through **TS2′** to give **M3′** and of **M2′-big** through **TS2′-big** to give **M3′-big** due to a pronounced stabilization at the intermediates **M2′** and **M2′-big** when entropic effects are included. The values assessed for these energy barriers at UB3LYP/6-31 + G(d) are 65.0 and 92.1 kcal mol^{-1} for the small system and 82.5 and 108.4 kcal mol^{-1} for the large system at 473.15 and 1,073.15 K, respectively. At UM06-2X/6-31 + G(d) these barriers amounts to 54.6 and 81.0 kcal mol^{-1} for the small system, and to 79.4 and 107.2 kcal mol^{-1} for the large one. Although these energetic values are higher than those experimentally reported for the NO reduction by different carbonaceous materials [12, 35–38]; the rise of the rate-determining Gibbs energy barrier when going from the lower temperature regime to the higher one is in accordance with experimental trends. Furthermore, the elucidated mechanism provides a satisfactory explanation of the experimental data [5]. At low temperatures the mean energy available to the reactants is not sufficient to overcome the high-energy barrier corresponding to the rate-determining step, as a result the gasification of the char surface (CO_2 emission) does not take place, the formation of N_2 and oxygen complexes on the surface of the carbonaceous material being the final products of the reaction. In contrast, at high temperatures the reactants have enough energy to surmount this barrier giving rise to oxygen and nitrogen complexes on the carbon surface, with the formation of N_2 and CO_2 as reduction products, in agreement with the experimental data [5]. In accordance with this, on the basis of the transition state theory equation the reaction rate calculated with the M06 results at 1,073.15 K is about 10^{15} times greater than that at 473.15 K for the large system (10^9 for the small model). This is in agreement with the experimental fact that, in general, the reaction rate of the NO heterogeneous reduction increases as the reaction temperature is raised [36, 37, 39].

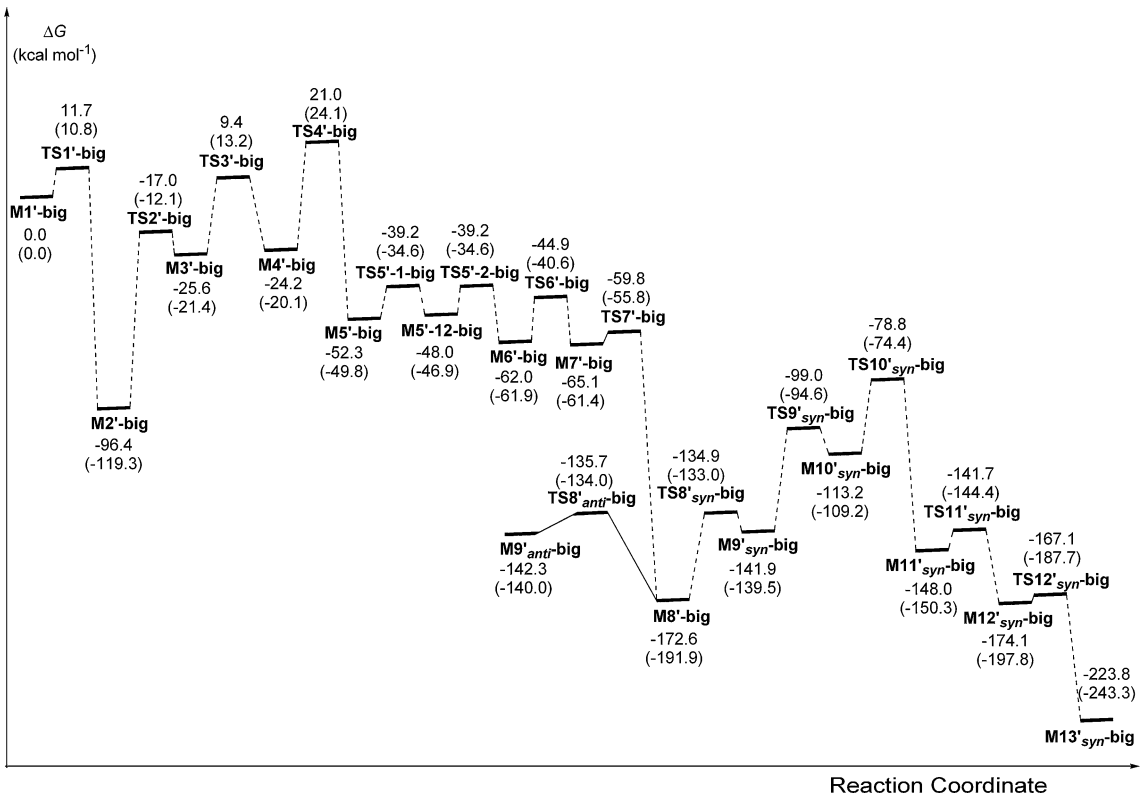

Fig. 7 UM06-2X/6-31 + G(d) Gibbs energy profiles at 473.15 and 1,073.15 K (*in parenthesis*) for the reaction between the ten benzene radical and NO

Considering the small model, it should be noted that the theoretical Gibbs energy pathways leading to **M13′**$_{syn}$ (N_2 emission) and **M12′**$_{anti}$ (N_2O emission) from **M1′** present the same rate-determining step, which corresponds to the evolution from **M2′** to **M3′** and has an energy barrier of 92.1 (B3LYP) and 81.0 (M06-2X) kcal mol^{-1} at 1,073.15 K. In addition, at this high temperature both processes from **M8′** display practically the same Gibbs energy barrier for the rate-determining step, 59.8 (B3LYP) and 62.3 kcal mol^{-1} (M06-2X) for the evolution of **M8′** to **M9′**$_{anti}$, and 59.7 (B3LYP) and 62.5 (M06-2X) kcal mol^{-1} for the evolution of **M8′** to **M9′**$_{syn}$. However, given that **M12′**$_{anti}$ presents a smaller barrier than **M13′**$_{syn}$ for its reverse evolution to **M8′** [66.3 (B3LYP) and 61.1 (M06-2X) kcal mol^{-1} for the transition from **M12′**$_{anti}$ to **M11′**$_{anti}$, and 80 (B3LYP) and 83.7 (M06-2X) kcal mol^{-1} for the transition from **M11′**$_{syn}$ to **M10′**$_{syn}$], and that **M13′**$_{syn}$, is 59.6 kcal mol^{-1} (B3LYP) and 59.7 (M06-2X) kcal mol^{-1} more stable than **M12′**$_{anti}$, the N_2 emission route appears to be the most favored one. The absence of N_2O elimination becomes completely clear when considering the large model, as the *anti* reaction path is truncated at **M9′**$_{anti}$**-big**.

The theoretical computations predict that two sources of N_2 formation coexist at high temperatures in accordance with experimental findings [5]. On the one hand, as a result of the breaking of both N–O bonds from the initial complex, **M1′** or **M1′-big**, and on the other, as a result of the evolution of the intermediates formed by the NO molecules attacking the nitrogen complexes generated on the carbon surface at **M8′** or **M8′-big**.

4 Conclusion

In the present work, mechanistic routes for the heterogeneous reduction of nitric oxide on anthracene radical and on a ten benzene monoradical, as models of carbonaceous materials which have active sites, were reported. B3LYP and M06-2X DFT functionals were used in the calculations. Both explain experimental results displayed below, but M06-2X yields higher energy barriers all along the energy profiles except for the limiting step. The same trend was obtained at ROMP2-FC/6-31 + G(d) theory level.

The mechanism found provides a suitable explanation for the experimental evidences, both at the low and high temperature regimes, and shows the important role played by temperature and the oxygen and nitrogen surface complexes, generated in the carbonaceous material as intermediate steps of the mechanism, in the reduction process.

According to the computational study presented in this work, at low temperatures, the breaking of both N–O bonds from the $(NO)_2$ dimer initially chemisorbed on the char surface generates N_2 together with oxygen surface complexes, and CO_2 emission does not take place. However, at high temperatures, N_2 and CO_2 are the observed reduction products and two sources of N_2 formation coexist. Thus, the generation of N_2 at the high temperature regime can proceed from a mechanism analogous to that described for the low-temperature regime, or from the evolution of the precursor formed when new NO molecules attack the intermediate nitrogen surface complexes on the carbonaceous material. The description of the carbonaceous surface through the large model confirms the absence of N_2O release in the reduction of NO on carbon surfaces.

References

1. Ph Chambrion, Kyotani T, Tomita A (1998) Energy Fuels 12:416–421
2. Teng H, Suuberg EM (1993) J Phys Chem 97:478–483
3. Illán-Gómez MJ, Linares-Solano A, Radovic LR, Salinas-Martínez de Lecea C (1996) Energy Fuels 10:158–168
4. Xiao B, Boudou JP, Thomas KM (2005) Langmuir 21:3400–3409
5. Pevida C, Arenillas A, Rubiera F, Pis JJ (2007) Fuel 86:41–49
6. Smith RN, Swinehart J, Lesnini D (1959) J Phys Chem 63:544–547
7. Arenillas A, Pevida C, Rubiera F, García R, Pis JJ (2004) J Anal Appl Pyrol 71:747–763
8. Arenillas A, Pevida C, Rubiera F, Pis JJ (2003) Fuel 82:2001–2006
9. Arenillas A, Pevida C, Rubiera F, Palacios JM, Navarrete R, Denoyel R, Rouquerol J, Pis JJ (2004) Carbon 42:1339–1344
10. Pevida C (2004) PhD Thesis, University of Oviedo
11. Pevida C, Arenillas A, Rubiera F, Pis JJ (2005) Fuel 84:2275–2279
12. Teng HS, Suuberg EM, Calo JM (1992) Energy and Fuels 6:398–406
13. Iaconis E, Illas F, Russo N, Toscano M (1988) Gazz Chim Ital 118:603–605
14. Ninomiya Y, Kato H, Koketsu J (1995) In: Pajares JA, Tascon JMD (eds) Coal science, vol 1. Proceeding of the 8th international conference on coal science. Elsevier, Amsterdam, pp 747–750
15. Chen N, Yang RT (1998) J Phys Chem A 102:6348–6356
16. Kyotani T, Tomita A (1999) J Phys Chem B 103:3434–3441
17. Montoya A, Truong TN, Sarofim AF (2000) J Phys Chem A 104:6108–6110
18. Montoya A, Truong TN, Sarofim AF (2000) J Phys Chem A 104:8409–8417
19. Gaussian 03, Revision B.04, Frisch MJ, Trucks GW, Schlegel HB, Scuseria GE, Robb MA, Cheeseman JR, Montgomery JA Jr, Vreven T, Kudin KN, Burant JC, Millam JM, Iyengar S, Tomasi J, Barone V, Mennucci B, Cossi M, Scalmani G, Rega N, Petersson GA, Nakatsuji H, Hada M, Ehara M, Toyota K, Fukuda R, Hasegawa J, Ishida M, Nakajima T, Honda Y, Kitao O, Nakai H, Klene M, Li X, Knox JE, Hratchian HP, Cross J B, Bakken V, Adamo C, Jaramillo J, Gomperts R, Stratmann RE, Yazyev O, Austin AJ, Cammi R, Pomelli C, Ochterski JW, Ayala PY, Morokuma K, Voth GA, Salvador P, Dannenberg JJ, Zakrzewski VG, Dapprich S, Daniels AD, Strain MC, Farkas O, Malick DK, Rabuck AD, Raghavachari K, Foresman JB, Ortiz JV, Cui Q, Baboul AG, Clifford S, Cioslowski J, Stefanov BB, Liu G, Liashenko A, Piskorz P, Komaromi I, Martin RL, Fox DJ, Keith T, Al-Laham MA, Peng CY, Nanayakkara A, Challacombe M, Gill PMW, Johnson B, Chen W, Wong MW, Gonzalez C, Pople JA (2004) Gaussian Inc., Wallingford, CT
20. Gaussian 09, Revision A.1, Frisch MJ, Trucks GW, Schlegel HB, Scuseria, GE, Robb MA, Cheeseman JR, Scalmani G, Barone V, Mennucci B, Petersson GA, Nakatsuji H, Caricato M, Li X, Hratchian HP, Izmaylov AF, Bloino J, Zheng G, Sonnenberg JL, Hada M, Ehara M, Toyota K, Fukuda R, Hasegawa J, Ishida M, Nakajima T, Honda Y, Kitao O, Nakai H, Vreven T, Montgomery JA Jr, Peralta JE, Ogliaro F, Bearpark M, Heyd JJ, Brothers E, Kudin KN, Staroverov VN, Kobayashi R, Normand J, Raghavachari K, Rendell A, Burant JC, Iyengar SS, Tomasi J, Cossi M, Rega N, Millam JM, Klene M, Knox JE, Cross JB, Bakken V, Adamo C, Jaramillo J, Gomperts R, Stratmann RE, Yazyev O, Austin AJ, Cammi R, Pomelli C, Ochterski JW, Martin RL, Morokuma K, Zakrzewski VG, Voth GA, Salvador P, Dannenberg JJ, Dapprich S, Daniels AD, Farkas O, Foresman JB, Ortiz JV, Cioslowski J, Fox DJ (2009) Gaussian Inc., Wallingford, CT
21. Becke AD (1993) J Chem Phys 98:5648–5652
22. Becke AD (1988) Phys Rev A 38:3098–3100
23. Lee CT, Yang WT, Parr RG (1988) Phys Rev A 37:785–789
24. Zhao Y, Truhlar DG (2008) Theor Chem Acc 120:215–241
25. Hehre WJ, Radom L, Pople JA, von Schleyer PR (1986) Ab initio molecular orbital theory. New York, Wiley
26. Schlegel HB (1982) J Comput Chem 3:214–218
27. Sousa SF, Fernandes PA, Ramos MJ (2007) J Phys Chem A 111:10439–10452
28. Zhao Y, Truhlar DG (2008) Acc Chem Res 41:157–167
29. González C, Schlegel HB (1989) J Chem Phys 90:2154–2161
30. González C, Schlegel HB (1990) J Phys Chem 84:5523–5527
31. Boys SF, Bernardi F (1970) Mol Phys 19:553–566
32. Simon S, Duran M, Dannenberg JJ (1996) J Chem Phys 105:11024–11031
33. McQuarrie DA (1986) Statistical mechanics. Harper and Row, New York
34. Dubsky J, Beran S (1979) Surf Sci 79:53–62
35. Chan LK, Sarofim AF, Beek JM (1983) Combust Flame 52:37–45
36. Aarna I, Suuberg EM (1997) Fuel 76:475–491
37. Li YH, Lu GQ, Rudolph V (1998) Chem Eng Sci 53:1–26
38. Schönenbeck C, Gadiou R, Schwartz D (2004) Fuel 83:443–450
39. Lu P, Xu SR, Zhu XM (2009) Fuel 88:110–115